
# Electrochemical Approach for Advanced Flow Reactors via Additive Manufacturing of High Surface Area Ti-6Al-4V Anode

ChemElectroChem

Research Article
doi.org/10.1002/celc.202300319

Chemistry Europe
European Chemical Societies Publishing

www.chemelectrochem.org

Special Collection

# Electrochemical Approach for Advanced Flow Reactors via Additive Manufacturing of High Surface Area Ti-6Al-4V Anode

Mohammad Reza Bilesan,*[a] Meghdad Yazdani,[b] Mathilde Luneau,[c] Gerard Montserrat-Sisó,[d] Björn Wickman,[d] and Eveliina Repo[a]

Electrochemical processes use expensive noble metal-based anodes which limit industrial implementation. In this study, a noble-metal-free Ti-6Al-4V anode is introduced in an advanced flow reactor. We demonstrate that the 3D additively manufactured electrode can provide a more projected surface area and facilitate anodic reactions under controlled electrolyte conditions. Alkaline NaOH and KOH electrolytes act as anodic electrolytes that are toxic compounds-free and enable corrosion control. Impedance and voltammetry responses to electrochemical reactions are studied. The electrochemical active surface area of the 4 rods scaffold geometry is 42 times higher than a flat plate anode. Therefore, improved charge transfer is achieved in the flow reactor incorporating the 3D Ti-6Al-4V electrode due to the increased surface area and wettability. The structure of almost non-conductive passivation on a flat plate anode is changed to unstable passivation due to the 3D scaffold structure. This enables effective charge transfer of 911 mA cm$^{-2}$ at higher potentials up to 5 V for 1.5 M KOH in a non-flow condition. Furthermore, a 1 M KOH solution delays metal ion dissolution from the anode surface by acting as a corrosion-controlling medium. 3D Ti-6Al-4V is likely to be an affordable alternative anode in alkaline environmentally friendly electrochemical applications.

## Introduction

Electrochemical processes have raised significant interest in recent years as a selective and more environmentally friendly alternative to conventional chemical methods.[1–3] To make electrochemical processes viable, highly efficient anodes are necessary to enhance the anodic reaction.[4] Noble metal-based anodes are widely used in such electrochemical processes.[5] However, several factors hinder their practical applications in electrochemical reactors, such as overpricing, limited supply, and poor stability of noble metals.[6] In order to overcome such limitations, electrochemical reactors with noble-metal-free electrodes in alkaline media need to be developed.

Electrochemical flow reactors have been investigated for metal recovery in recent years.[6,7] In a flow reactor configuration, electrolyte storage in external tanks limits deactivation of the electrodes by preventing undesired chemical and physical changes to the electrodes over time. This leads to increased reactor performance and reduced maintenance requirements, making this technology promising for large-scale applications.[8] By designing compartments separately and using exchange membranes, preferred anodic reactions can be achieved. Conventional anodic reactions can be replaced with oxygen evolution at the anode, which is more environmentally friendly. Consequently, noble metal-free anodes must be developed at a low cost and with an easy manufacturing process for electrochemical applications.

Laser powder bed fusion (L-PBF) is a promising additive manufacturing method to achieve optimal performance.[9] In L-PBF, the thickness, mesh size, strand size, and profile of materials can all be carefully tuned. Control over these key parameters results in improved mass transport properties which are crucial in flow reactors. In the past, scaffold-like structures developed by L-PBF have shown enhanced electrode performance by presenting high volumetric area electrodes with low-pressure drop in reactors with flow-through electrodes.[6] The L-PBF electrodes have shown superior mass transport to meshes,

[a] M. Reza Bilesan, Prof. E. Repo
Department of Separation Science
School of Engineering Science
LUT University
FI-53850, Lappeenranta (Finland)
E-mail: Mohammad.Reza.Bilesan@lut.fi
mr.bilesan@gmail.com

[b] M. Yazdani
School of Metallurgy and Materials Engineering
College of Engineering
University of Tehran
P.O. Box 11365-4563, Tehran (Iran)

[c] Asst. Prof. M. Luneau
Department of Chemistry
Chalmers University of Technology
412 96, Gothenburg (Sweden)

[d] Dr. G. Montserrat-Sisó, Assoc. Prof. B. Wickman
Department of Physics
Chalmers University of Technology
412 96, Gothenburg (Sweden)

Supporting information for this article is available on the WWW under https://doi.org/10.1002/celc.202300319

This publication is part of a Special Collection on Holistic Development of Electrochemical Processes for Industrial Systems

foams, and conventional planar electrodes.[10] Such improved mass transport combined with a large surface area and controlled porosity enhances reaction rates at the electrode surface.[11]

Material selection is significant for an electrode as it determines its electrical conductivity and catalytic activity. Ti-6Al-4V alloys manufactured by L-PBF are promising noble-metal-free alternatives to anode electrodes in flow reactors. The anodic behavior of Ti-6Al-4V alloys manufactured by additive manufacturing has been investigated in solutions such as NaCl, HCl, NaOH, $H_2SO_4$, Hank's artificial body fluid, and phosphate-buffered saline solutions.[12–15] Hence, the Ti-6Al-4V alloy is one of the most widely used Ti-based alloys due to its high mechanical strength, corrosion resistance, exceptional biomedical applications, and engineering structures applications.[16,17] However, the superior mechanical strength associated with Ti-6Al-4V results in high costs and difficulties in manufacturing substantial and complex structural components using conventional manufacturing methods.[18]

High density of active sites and high electrode surface area are essential to enhance anodic reactions. Recent studies reported that higher surface areas could be achieved by soaking Ti powders in KOH than in NaOH at different temperatures.[19] The alkali-treated Ti parts led to the formation of hydrated titanium layers, which change from a hydrophobic to hydrophilic surface.[20] On the other hand, the wettability of the Ti surfaces can be enhanced by NaOH or KOH treatments. Consequently, these physical modifications could provide a practical advantage for the complex porous structure by improving bubble removal during anodic reactions.[21] In other words, increased electrode wettability enables easier access to reactive regions of a porous electrode for electroactive species.

Alkaline electrolytes are favorable because they reduce the corrosion rates of noble and non-noble metal-based electrodes.[22] Titanium alloys are stable enough to be utilized in alkaline media, with corrosion rates of ~0.07–0.16 mm/year at 110 °C using 7.5 M NaOH solution.[23] The corrosion rate is low at high temperatures and in highly concentrated NaOH and KOH solutions. Since corrosion occurs at temperatures approximately above 80 °C in NaOH (pH > 12) or applied potentials lower than −0.7 V (SCE), hydrogen embrittlement appears in the form of brittle TiH precipitations in the alloy as there is a significant increase in hydrogen diffusion rate.[24] The stable, passive oxide layer formed on the Ti-6Al-4V alloy surface is well-known for its outstanding corrosion resistance in biofluids.[25,26] Previous studies stated that its oxide layer primarily consists of $TiO_2$ with minor amounts of TiO and $Ti_2O_3$ near the metal-oxide interface. In addition, aluminum and vanadium oxides were identified in the passive layer. Higher aluminum (26 wt.%) and lower vanadium (1 wt.%) content were measured compared to the initial alloy composition.[27–30]

Local heating and internal compressive pressures provided by charge transfer are the major causes of anodic titanium oxide film crystallization at the surface.[31,32] Anodic oxide crystallization on titanium is a slow, thermally driven process that can be expedited by increasing the current density, increasing the electrode potential on the anode side (i.e., making it more oxidative) or increasing the electrolyte temperature.[33] Furthermore, crystallization is often followed by amorphous anodic titanium oxide film deformation with lower ion conductivity. Potentiostatic conditions can produce crystalline grains that facilitate ionic conductivity.[34,35] Regarding the oxygen reduction reaction (ORR) activity, the active site for the ORR might be a low valence state of titanium ions, $Ti^{3+}$.[36] Therefore, distortions in the anatase, or brookite phases are favorable as they improve ORR activity.

The microstructure of L-PBF manufactured materials, such as selective laser melting (SLM) produced alloys, exhibits a stressed and non-stabilized microstructure due to the specific scan strategies used in the SLM process. It is expected that the corrosion resistance of SLM-produced Ti-6Al-4V could be improved if the non-equilibrium acicular α′ martensitic phase could be transformed into the α martensitic phase.[37] However, this non-stabilized stressed microstructure can be considered an advantage for complicated 3D surfaces as it can prevent the formation of a uniform passive layer by creating more surface defects, which can be considered active sites. The designed anode needs to provide an unstable passive layer that enables the anode to become more conductive. This is done by breaking the oxide forms of surface species. An unstable passive layer can provide more defects and porosities which ease the path of the electrons path toward the electrode surface. This is done by increasing the surface area and inhibiting oxide layer propagation at the surface.[38]

Although several studies have examined Ti-6Al-4V alloy surface treatment and biomaterial functionality, 3D-structured Ti-6Al-4V electrodes can provide novel functionality in electrochemical flow reactors, thus enhancing the anodic process at a reasonable cost. In this work, we demonstrate that additive manufacturing provides high projected surface area without pressure drop at the anode surface. This is highly preferable for flow reactors. 3D-designed Ti-6Al-4V can be used as a noble-free electrode with outstanding charge transfer and reasonable corrosion resistance suitable for flow reactors. AMed Ti-6Al-4V electrodes are fabricated using SLM, leading to a 3D electrode with controlled porosity that facilitates mass transport. When an alkaline solution and a hydrophilic physical modification are combined, bubbles can be generated from electrode surfaces with greater efficiency.[39] The electrochemical anodic behavior of the Ti-6Al-4V alloy was evaluated based on static and dynamic electrochemical conditions. The effect of KOH and NaOH electrolytes on performance and alloy dissolution is thoroughly studied by combining electrochemical tests and ex-situ X-ray photoelectron spectroscopy (XPS), scanning electron microscope (SEM), and 3D laser scanning microscopy techniques. All these feasibility evaluations were performed to determine the optimum charge transfer under corrosion-controlled conditions for the 3D Ti-6Al-4V alloy as a highly affordable anode. By using a highly asymmetric anode, the mass transfer resistance inside the anode may be reduced. This may result in less concentration polarization inside the anode and more efficient generation of anodic current in flow reactor stacks.

## Results and Discussion

The 3D scaffold structure presents a significantly higher ECSA than the flat plate anode. Voltammetry at different scan rates in the capacitive region was used to determine the ECSA. According to the data derived from (Figures 1a and b), the double layer capacitance $C_{dl}$ of the scaffold is determined to be $5.11\times10^{-4}$, and the $C_{dl}$ of the plate is defined to be $1.21\times10^{-5}$. Therefore, the ECSA of the scaffold is 42 times more than the plate. The high value in ECSA means the anodic electrochemical reaction (OER) was significantly improved.

The polarization curves and corrosion behaviors of the electrodes vary with KOH concentration (Figure 2a). The Tafel curves present two regimes: ion dissolution and OER on the anodic and cathodic sides. (Figure 2a). The corrosion potential ($E_{corr}$) of the samples in KOH solutions initially increased with increased $OH^-$ concentrations. The $E_{corr}$ demonstrates the thermodynamic behavior of electrochemical reactions. This increase in corrosion rate ($I_{corr}$) is evident from the extracted the polarization curve results (Figure 2c). The corrosion rate decreased to 1.5 M KOH. This decline indicates a drop in kinetics of the anodic reactions. This can be due to the presence of higher alkalinity and hydroxide phase formations at the surface of the electrode. this makes it more corrosion resistance. Therefore, the initiation and feasibility of anodic reactions are facilitated when KOH concentrations increase from 0.5 to 1 M KOH. However, at higher concentrations (1.5 M KOH), the activation energy is increased, and the anodic reaction becomes more challenging.

In the case of NaOH, the corrosion rate decreased with increasing NaOH concentration (Figure 2b). The decline implies that there can be a drop in anodic reaction kinetics in the cell. The remarkable point is that the magnified $E_{corr}$ from 0.5 to 1 M NaOH demonstrates the difficulty in corrosion, and then the

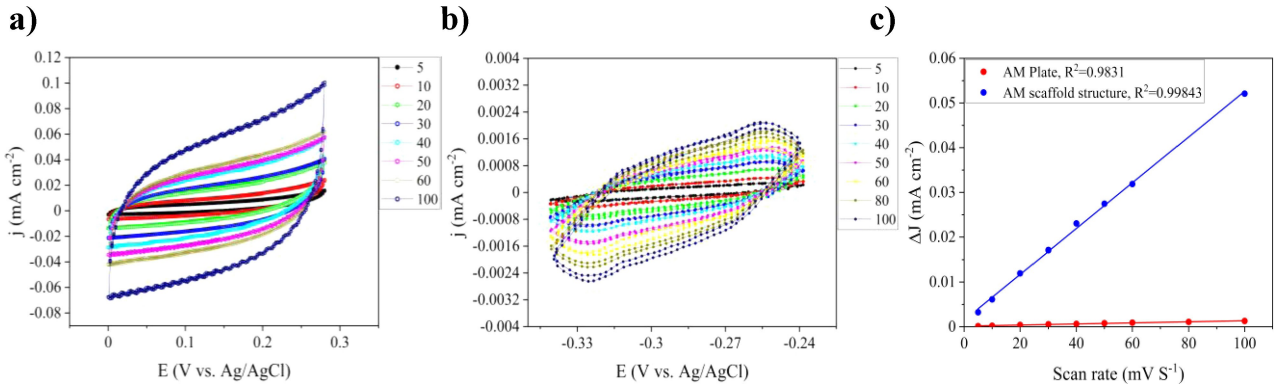


**Figure 1.** CV curves of a) AM diamond 4 rods, b) plate in scan rates from 5 to 100 mV $s^{-1}$, c) charging current density at the applied scan rates.

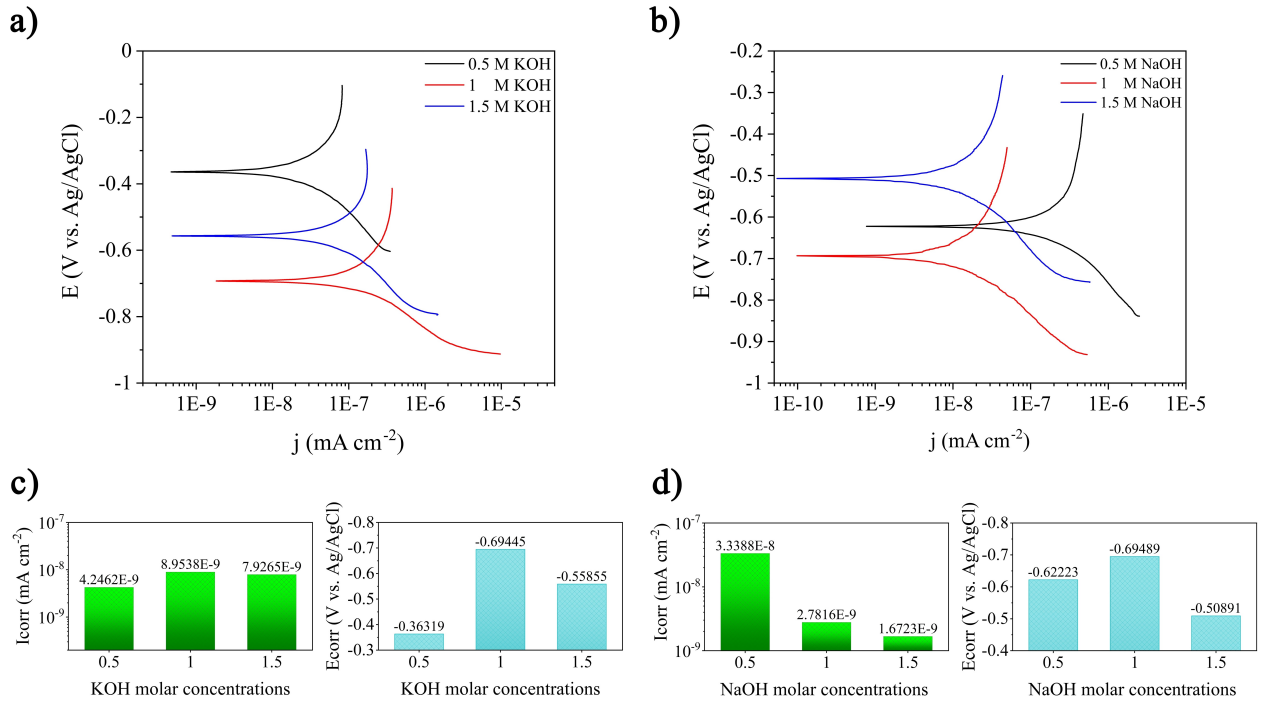


**Figure 2.** a and b) Tafel curves (at 0.5 mV $s^{-1}$ scan rate). c and d) $I_{corr}$, and $E_{corr}$ excluded from polarization curves.

drop at the higher concentration (1.5 M NaOH) showed a straightforward corrosive behavior from the thermodynamic viewpoint (Figure 2d). is thus predicted by thermodynamics and kinetics predict a simple anodic reaction due to NaOH concentration increase.

LSV measurements show that the sample shifted from the passivation zone and entered a transpassive zone when the anode potential rose beyond the passivation potential (Figure 3a and 3b). The 1.5 M KOH and NaOH solutions yielded ~285 and ~100 mA cm$^{-2}$ at 3 V as the highest current densities, respectively (Figure 3b). Active dissolution on the alloy surface was initiated by $OH^-$ breakdown on the passive layer. This is due to absorbing anions at the metal interface oxide layer. As the potential increased, the anode current density increased further, and the oxide layer chemically disintegrated. This resulted in micro-defects[42] or a tendency to form porous and uneven oxide layers to improve charge transfer through cracked oxide layers. Furthermore, for 0.5 and 1 M KOH, 1.4 V vs. Ag/AgCl illustrates an optimum critical moment with maximum peaks at current densities of 25 and 38 mA cm$^{-2}$, respectively. The 1 M NaOH electrolyte recorded 49 mA cm$^{-2}$, while 0.5 M NaOH exhibited 33 mA cm$^{-2}$. The LSV curves showed current density oscillations, indicating the possibility of nucleation and further repassivation of unstable pits on the initial passive film to increase the resistance to charge transfer at higher potentials, which has been reported previously.[43] The current density for each specimen intensified with an accelerated slope when the potential increased. More current can be applied by increasing the potential beyond 3 V during the anodic process (Figure 3a). At higher potentials up to 5 V, 1.5 M KOH and NaOH solutions demonstrated 911 and 640 mA cm$^{-2}$, respectively. However, the passive layer on wrought Ti-6Al-4V plates plays almost a non-conductive role in alkaline solutions, which is a completely opposite phenomenon.[44] The considerable amount of charge transfer implies that the AM technique can be utilized for Ti-6Al-4V to introduce a suitable anode for OER reactions. Defects on the passive layer structure provide appropriate anodic electrical conductivity. Higher alkalinity can provide lower activation energy and/or applied polarization on the anode surface.

Nyquist plots show electrochemical impedance spectroscopy (EIS) measurements in KOH and NaOH solutions (0.5 M, 1 M, 1.5 M) at different concentrations (Figure 4a). The real impedances of the samples in KOH electrolytes were nearly higher than those of the samples in NaOH. The samples with the lowest real (Z′) and imaginary impedance (Z″) in a magnified portion displayed the comparable deviation of impedance in each electrolyte (Figure 4a). The data obtained from KOH solutions at steps 0.5 M to 1 M indicated that the real impedance was increased. This implies that the resistance of the 1 M KOH solution was greater than that of the other samples. The data interpretations confirm the real impedance is associated with all resistors in electrical circuits. The imaginary impedance is identified by other components such as capacitors.

Phase angle (φ) versus frequency was acquired from EIS measurements (Figure 4b). The presence of two hills or two time-constants of phase angles can be explained by the electrochemical behavior of the samples in the different alkaline solutions. Due to the different densities of the defects during passivation, this behavior can be attributed to the two densities of the different defects. The final produced layer is a double layer with a less compact defect layer near the substrate. It also has a more compact defect layer exposed to the electrolyte. Therefore, the passive layer has two layers on the surface. The top layer intersection between passive layer and solution is attributed to the electrode surface and its structural defects. Thus, there would be a different electrochemical behavior at the intersection of lower layer, between the metal and passive layers. By increasing the KOH concentration from 0.5 M to 1.5 M, since the first hill was more prominent than the second, it means that the lower layer has a low density of defects.[45–47] Additionally, The NaOH solutions follow a similar two-hill pattern, with one hill being more significant than the other. The corresponding characteristics of Bode plots for Z′ and Z″ showed the impedance modules (Figure 4c). For each fre-

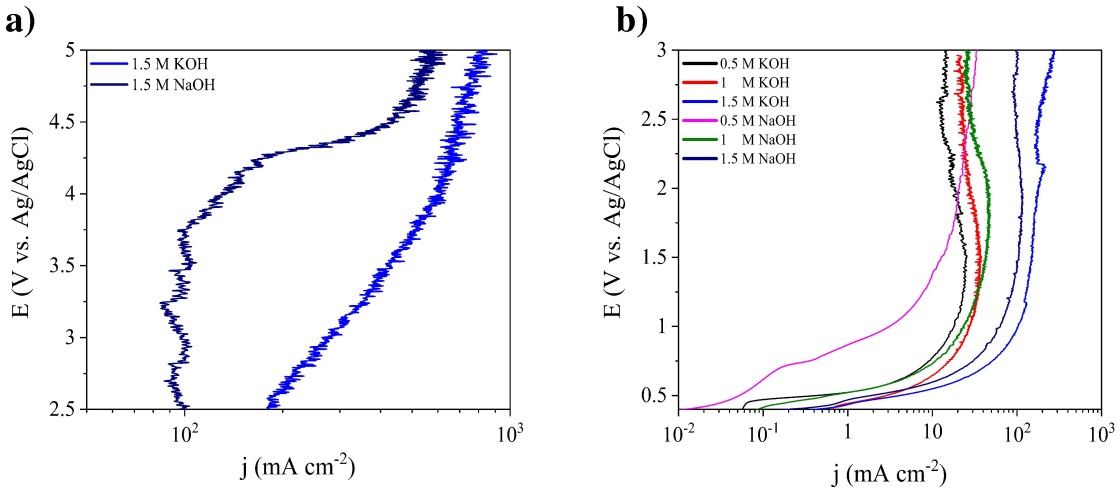


**Figure 3.** a and b) the OER LSV plots of the AM diamond 4 rods electrodes (at 2 mV s$^{-1}$ scan rate).

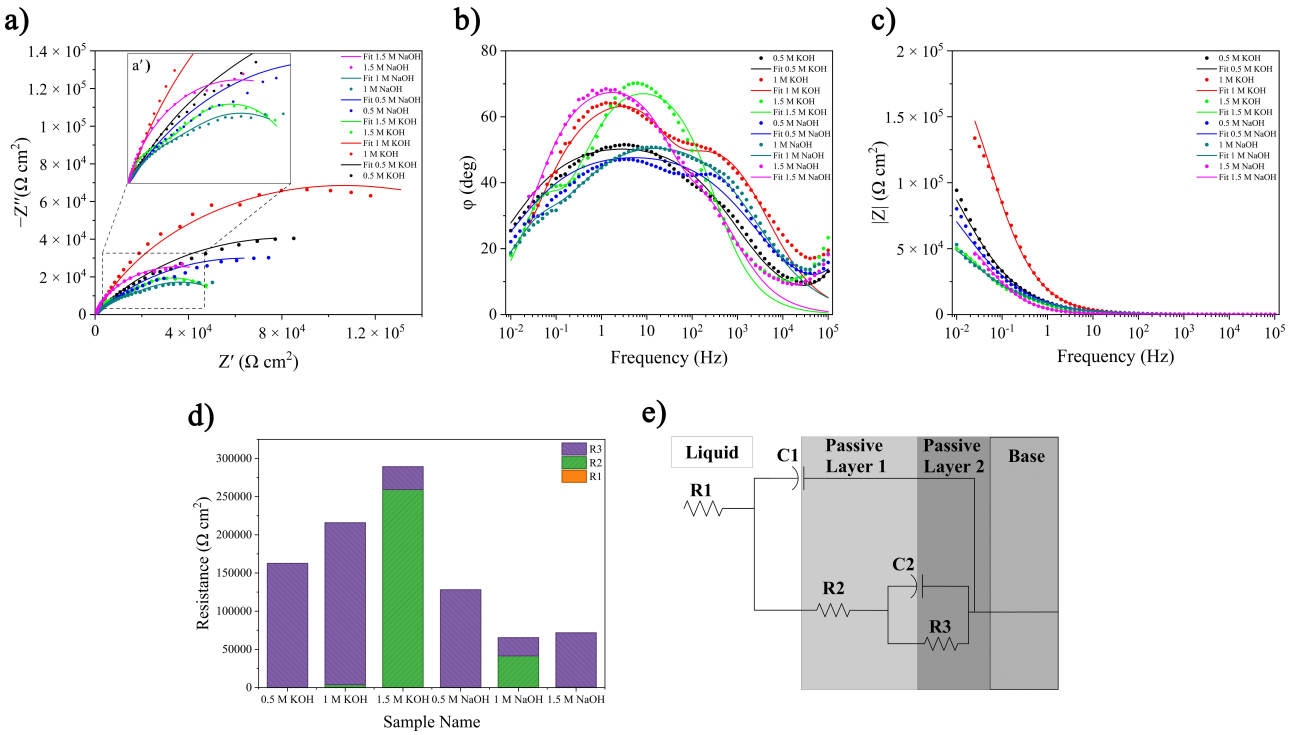


**Figure 4.** a) Nyquist plots, b) Bode angle plots per frequency, c) Bode phase per frequency, d) The interpreted EIS electrical elements acquired at various concentrations and alkaline solutions, and e) The schematic of electrical equivalent circuit.

quency, the impedance is defined by a vector of magnitude |Z| . All electrochemical behaviors were demonstrated in the Nyquist plots and approved in the Bode plots. The Bode plots indicate that the oxide film resistance and thickness were both increased for the samples from 0.5 to 1 M KOH. Additionally, 1 M NaOH and 1.5 M KOH solutions showed the lowest resistance compared to the others, which was proven by previous studies.[48] However, 1.5 M NaOH demonstrated moderately higher resistance than 1 M NaOH.

The EIS interprets all electrical elements as electrical equivalent (Figures 4d and 4e). The cumulative resistance of the electrodes immersed in NaOH was first decreased and at higher pH (1.5 M NaOH) the resistance increased. It should be noted that these results are consistent with the results obtained from the $I_{corr}$ intensity in the Tafel test. Because these two criteria are inversely related, the $I_{corr}$ reduces as the charge transfer resistance increases. Due to the ineffective behavior of the anodic branch, electrochemical impedance results are more accurate and reliable. However, these two criteria will always be interdependent in terms of behavior. The anodic reactions impact the $I_{corr}$ but do not affect the charge transfer resistance. Therefore, based on the KOH Tafel and impedance measurements in the open circuit potential, it is possible to conclude that the KOH sample immersed in a concentration of 1 M will be the suitable sample for use as an anode. In addition, as NaOH concentration increases, resistance decreases approximately. A 1.5 M NaOH concentration would provide the most favorable anodic behavior in all these samples.

The novel DEIS method tracks corrosion dynamics by evaluating electrical properties of an equivalent circuit. The DEIS spectra achieved at 1.5 M NaOH, 1 M KOH, and 1.5 M KOH in the potential range between OCP and 2 V are presented (Figure 5). There is a semicircle pattern in the high-frequency range and a tail in the low-frequency range (Figures 5a–c). Each semicircle corresponds to the charge transfer resistance (Rct) related to the interface between electrodes and electrolytes. The Rct is determined by the electrode kinetics. The Nyquist spectra demonstrated a potential dependence behavior of Rct within the difference in the potentials. At higher potentials, magnitude of high-frequency semicircle decreased, and the flattened tail was terminated. Based on the fittings, Warburg behavior was seen at lower potentials and lower frequencies until 0.7 V for 1.5 M NaOH. Besides, 1 M and 1.5 M KOH electrolytes follow Warburg behavior until 0.5 V. The Nyquist spectra change at higher potentials. All the samples showed a decrease in the real and imaginary impedance values by changing the potential toward higher values (after 0 V, until 2 V). As more $Ti^{3+}$ defects are present on the surface, electron donors, in the form of oxygen vacancies, increase significantly in the passive film. As a result, the Rct decreases. Hence, this expansion in defects numbers lowered real and imaginary Z.

For all the electrolytes studied, the Bode magnitude graphs were comparable (Figures 5d–f). The Bode plot for 1.5 M NaOH demonstrated a high |Z| value at low-frequencies (10–100 Hz) which dropped intensively at 0.2 V (Figure 5d). Across the voltage range higher than 0.2 V, the Bode magnitude remained constant, indicating a double layer map due to the resistive response of the electrolyte.[49] The highest value of |Z| near −0.2 V at the lowest frequency (10 Hz) represented a capacitive response, whereas a redox response was shown at the other

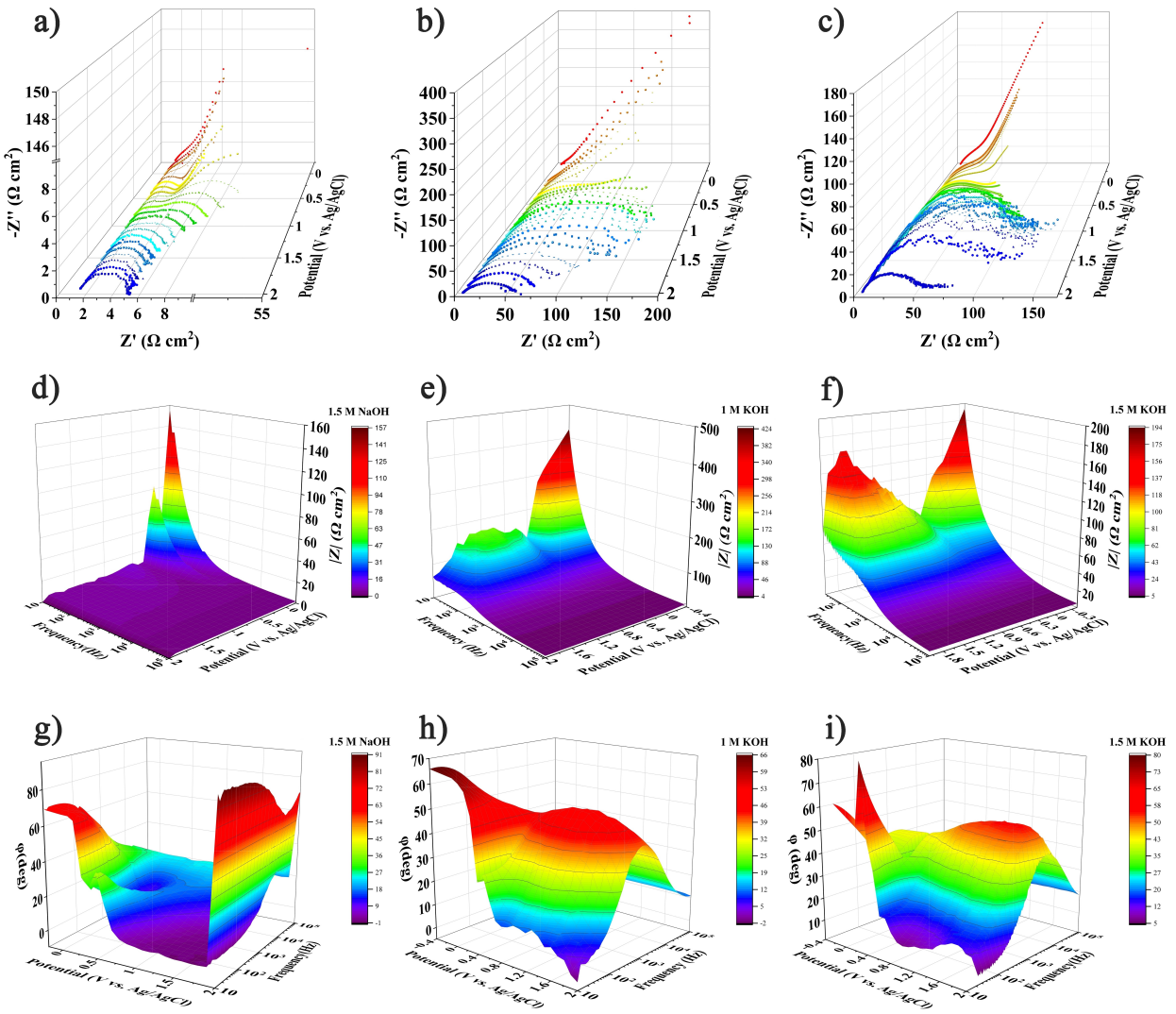


**Figure 5.** DEIS, bode phase, and bode angle plots of AM diamond 4 rods Ti-6Al-4V as a function of immersion in: a, d, and g) 1.5 M NaOH, b,e, and, h) 1 M KOH, and c, f, and i) 1.5 M KOH.

potentials. Capacitive responses prevented orbital coupling between the intercalated ions and the passive layer due to the oxide shell - particularly, the oxidized $Ti^{3+}$ ions from the double layers in the passive interlayers. Similar 3D Bode maps were observed for the 1 M and 1.5 M KOH solutions (Figures 5e and f). At low-frequencies (10–100 Hz), the Bode plots for 1 M KOH and 1.5 M KOH exhibited significant $|Z|$ values of 425 $\Omega cm^2$ and 193 $\Omega cm^2$, respectively, which fell rapidly at 0.4 V. Later, a mild slope of $|Z|$ between 0.4–1.6 V and 0.4–1.9 V indicated capacitive behavior at the low frequencies (10–100 Hz) for 1 M KOH and 1.5 M KOH, respectively. At higher potentials over 1.6 V for 1 M KOH and 1.9 V for 1.5 M KOH, the $|Z|$ value reduced until 2 V, which indicates redox behavior of KOH solutions at higher potentials. Due to the combined effects of capacitive and redox processes occurring at different potentials, these findings reveal that the 1 M and 1.5 M KOH samples have complex charge transfer dynamics. The data on $-\varphi$ versus frequency can be used to determine thelimiting kinetics rates for charge transfer. For pure resistive response, phase angle is 0°, for capacitive response it is 90°, and for diffusion restricted response it is 45°.

At potentials from −0.2 to 2 V, there were two unique zones in the Bode magnitude charts. At lower potentials than 0.2 V, Bode magnitude charts at lower frequencies ($10–10^2$ Hz) showed high phase angles of near 57°–69°, which dropped at 0.4 V (Figure 5g). This was due to the electrolyte resistance response. The phase angle map shows a dip valley at a potential of 0.4 V due to the basic nature of 1.5 M NaOH. There is a possibility of redox reactions (ion dissolution or partial dual behavior of the passive layer degradation). Furthermore, the electrode experiences a highly resistive response between 0.7–1.9 V at frequencies around $10–10^3$ Hz. The spectra had a linear slope throughout the broad frequency range at 1.9 V with a continuous horizontal 45° phase angle between 1.9 and 2 V. There is a high phase angle of 89° at 2 V, evidence of strong capacitive behavior. The phase angle close to 89° proves that passive films are relatively compact for 1.5 M NaOH. A high phase angle of near 65° at 10 Hz frequency, which drops at

0.4 V, proves resistive behavior the same as 1.5 M NaOH. This implies that the passive layer on the surface has been partially destroyed (Figure 5h). The initial high angle observation for all the studied samples, associated with a high $|Z|_{f\to 0}$ value could be correlated to the capacitive behavior of corrosion resistant materials like Ti-6Al-4V alloy.[48,50] The spectra had a dual linear slope throughout the broad low and high frequency range at 0.7–2 V. The phase angle drop at lower-frequency is a typical response behavior of surface film resistance, and the high-frequency one is caused by solution resistance.[49] In addition, pure capacitive behavior was seen at 1.9 V in the low and high-frequency range. The waterfall plot attained its maximum value at potentials approximately 1.1 V in the middle-frequency range (~450 Hz) and exhibited a significant resistive response at 52° (Figure 5h). A high resistive response (80°) and a capacitive response (5°) are observed at 0.1 V for 1.5 M KOH at both low and high frequencies (Figure 5i), respectively. The waterfall plot showed a maximum value at 55° in ~1700 Hz frequency. Consequently, slow redox processes occurred at low frequencies by reaching the maximum number of oxygen-bonded sites accessible for protonation reactions. This led to significant resistance at 1 and 1.5 M KOH.

The $-\varphi$ value in 1.5 M NaOH is smaller than in 1 and 1.5 M KOH solutions. This is due to the dominating redox reaction pathways at potentials 0.2–1.9 V for 1.5 M NaOH. However, a lower phase angle value at potentials higher than 1.9 V exhibited a capacitive response to 1 and 1.5 M KOH solutions. The presence of two hills showed two time-constants which manifested two different layers, one compact and the other porous layer (Figures 5g–i). The compact layer is close to the electrode surface, and its surface is denser. However, the density of layer is lower in the porous layer. Therefore, charge transfer is more straightforward in the porous layer.

Based on the simulated DEIS data, the sequence of all layers and electrical elements at the different applied potentials were modelled with electrical equivalents. The obtained overall values are modelled to make them readily comprehensible (Figure 6). The calculated Rct demonstrates a sharp decline from 0.6 V and 73 Ω cm$^2$ to 1.7 V at 19 Ω cm$^2$ for 1.5 M NaOH (Figure 6a). These results prove that the increase in active sites facilitates charge transfer within corrosive ion dissolution and the OER. In KOH solutions, different charge transfer behavior was observed. The 1 M KOH indicated a considerably higher resistance than 1.5 M NaOH (Figure 6b). This increase was moderate until 1 V at 185 Ω cm$^2$ and then gently declined until 2 V at 57 Ω cm$^2$. For 1.5 M KOH the peak at about 1.6 V at 173 Ω cm$^2$ demonstrate a continuous passive layer resistance with increasing potential until at 2 V an intensive drop to 71 Ω cm$^2$ occurred. A high peak at 1 M KOH compared to 1.5 M KOH (Figure 6c) is a sign of higher corrosion resistance. By increasing the potentials to higher values, the slope of potential declines sharply for 1.5 M KOH, showing an intensive corrosion behavior at higher potentials (2 V). Consequently, the 1 M KOH and 1.5 M NaOH were considered for phase structural behavior characterizations with XPS measurements.

The 3D morphology of the main electrodes designed for the advanced flow reactor was plotted using a 3D laser scanning microscope. The electrode morphology was investigated before and after 4 h of usage in the advanced flow reactor, treated with 1.5 M NaOH (Figures 7a and b). According to the qualitative topographical image of the untreated and treated AM electrodes, the color scales in both images are the same as the lower height levels are depicted in brighter colors than the higher levels. However, the differences in local topography gradients are noticeable. The scaffolds are less protruding after reaction.

The two specified horizontal distances between the selected joint spots are shown to indicate the profile variations on the scaffolds after 4 hours utilization (Figures 7c and d). The total height of the profile was 0.72 mm (Figure 7e), representing the vertical distance between the maximum profile peak height and the maximum profile valley depth over the assessed length. The mean value of the arithmetical mean height ($S_a$) and the mean maximum peak to valley ($S_z$) of the surface of three different areas were performed. The results demonstrated that the untreated AM electrode could provide a mean average $S_a$ of 110 μm regarding the four different selected zones (Table 1). Due to the anodic dissolution of the treated AM electrode, lower surface roughness was expected. The average mean $S_a$ was 77 μm. The oxide passive layer propagation and crystallization of a newly nuclei on the defects caused smoother growth of the oxide layer. Sz is defined as the sum of the highest peak altitude value and the largest pit depth value. When it comes to for the AM products, the provided surface

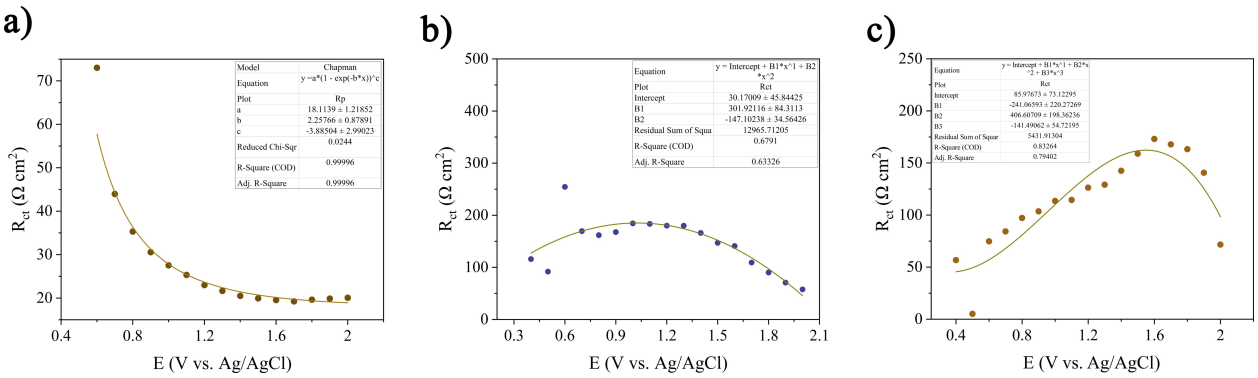


**Figure 6.** DEIS reports of AM diamond 4 rods Ti-6Al-4V as a function of immersion in: a) 1.5 M NaOH, b) 1 M KOH, and c) 1.5 M KOH.

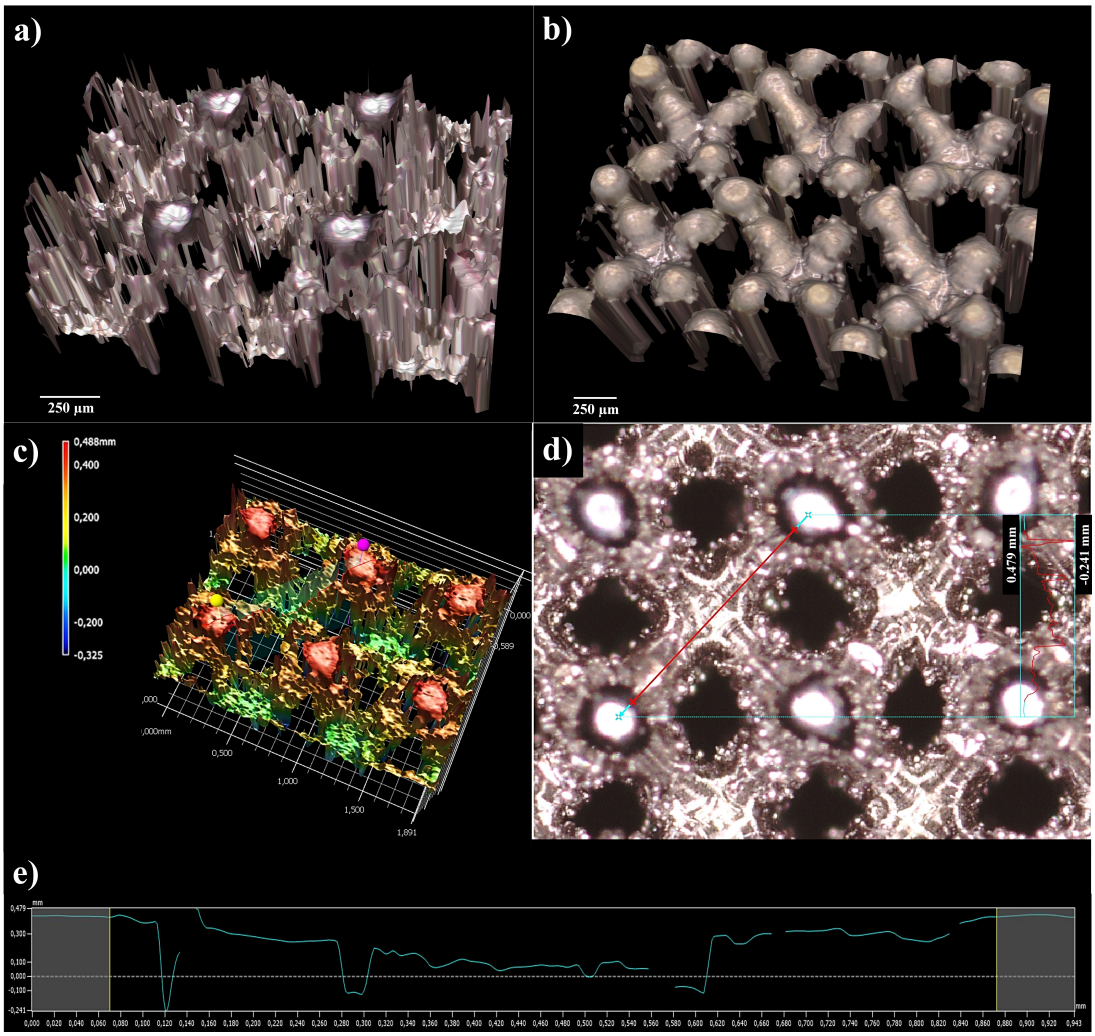


**Figure 7.** The 3D top view morphology of the AM diamond 4 rods Ti-6Al-4V, a) before, b) after 4 hours utilization in the advanced flow reactor, c and d) surface profiles measured at research points, and e) total height of the profile.

**Table 1.** Surface roughness between the AM electrode before and after the sever electrochemical conditions (1.5 M NaOH, 4 hours chronopotentiometry at 180 mA/cm$^2$).

| Name and Parameter | Mean 1st | Mean 2nd | Mean 3rd | Mean 4th | Mean Ave. |
|---|---|---|---|---|---|
| Untreated AM electrode $S_a$ | 81 µm | 123 µm | 119 µm | 120 µm | 110 µm |
| Treated AM electrode $S_a$ | 54 µm | 105 µm | 71 µm | 81 µm | 77 µm |
| Untreated AM electrode $S_z$ | 664 µm | 1191 µm | 4216 µm | 1184 µm | 1813 µm |
| Treated AM electrode $S_z$ | 807 µm | 1026 µm | 4234 µm | 1087 µm | 1788 µm |

contact angle is more related to $S_z$. The decrease in $S_z$ value from 1813 µm to 1788 µm means the contact angle for droplets will decrease, as stated in recent studies.[51] Therefore, samples treated with 1.5 M NaOH have a more hydrophilic surface. Therefore, electroactive species can reach the reactive regions of a porous electrode more easily when electrode wettability is increased. Bubble formation can be transferred more easily.

Ex-situ XPS measurements were used to investigate and determine the chemical composition of the oxide layers on the AM diamond 4 rod electrode used in the advanced flow reactor in Table S1. The deconvoluted Ti 2p spectra are shown in Figure 8.

In both samples tested in 1 M KOH and 1.5 M NaOH, two distinct regions were identified in accordance with flow directions footprints. Yellowish areas more prone to uniform flow were considered major reactive areas (Figure S1). The electrode treated in KOH appears to have a similar composition to the untreated material. In contrast, the electrode treated in NaOH appears to contain more than one Ti species. The untreated section only seems to contain $Ti^{4+}$ species at a

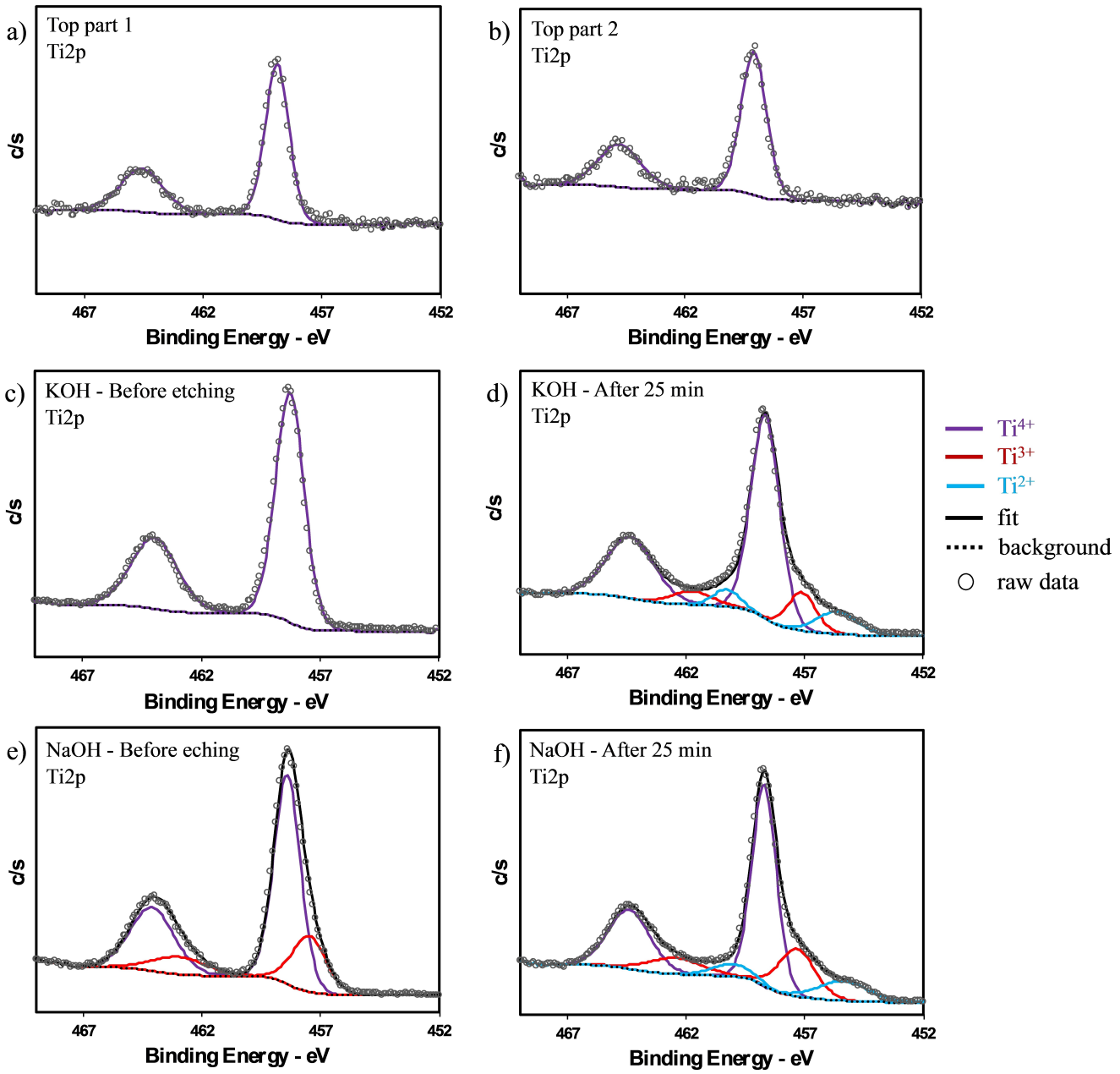


**Figure 8.** The XPS spectra of Ti 2p in the a) untreated point 1, b) untreated point 2, c) yellow region of the KOH sample as shown before etching the surface, and d) after 25 min of sputtering. e) XPS spectra of Ti 2p in the yellow region of the NaOH sample before etching the surface and f) after 25 min of sputtering.

binding energy of 458.6 ± 0.3 eV ($TiO_2$) (Figures 8a and b). The section treated in 1 M KOH (region 2) also showed $Ti^{4+}$ (Figure 8d) as the sole species albeit at a slightly higher binding energy than the untreated point (Figure 8c). Interestingly, the section treated in NaOH showed a major contribution from $Ti^{4+}$ but also a clear contribution at lower binding energies 457.3 ± 0.3 eV which could be attributed to $Ti^{3+}$ species (possibly $Ti_2O_3$) (Figures 8e and f). An increase in the $Ti^{3+}$ concentration in the NaOH sample could be related to crystallographic lattice distortion, which allows the reduction of more $Ti^{4+}$ available sites to $Ti^{3+}$.[35] The metastable crystalline anatase phase ($Ti^{4+}$) distortion could provide higher OER activity by producing $Ti^{3+}$ on the surface. The oxide distortion could increase the local current density of an anodic oxide layer. This facilitates crystallization due to local current density or local heating, according to a widely accepted interpretation.[52] Besides, the internal compressive stress produced by the SLM manufacturing method could be considered as another reason for titanium anodic oxide crystallization. This has been extensively studied in other research.[34,35] As a result, the more defects allow more crystalline phases to grow at the same time.

After 25 min of sputtering to etch the surface, the treated sections of both KOH and NaOH samples appear to contain three different Ti species: in addition to $Ti^{4+}$ and $Ti^{3+}$ species, another contribution at 455.6 ± 0.3 eV could be attributed to $Ti^{2+}$ species (Figures 9d and f). At the same depth, the passive

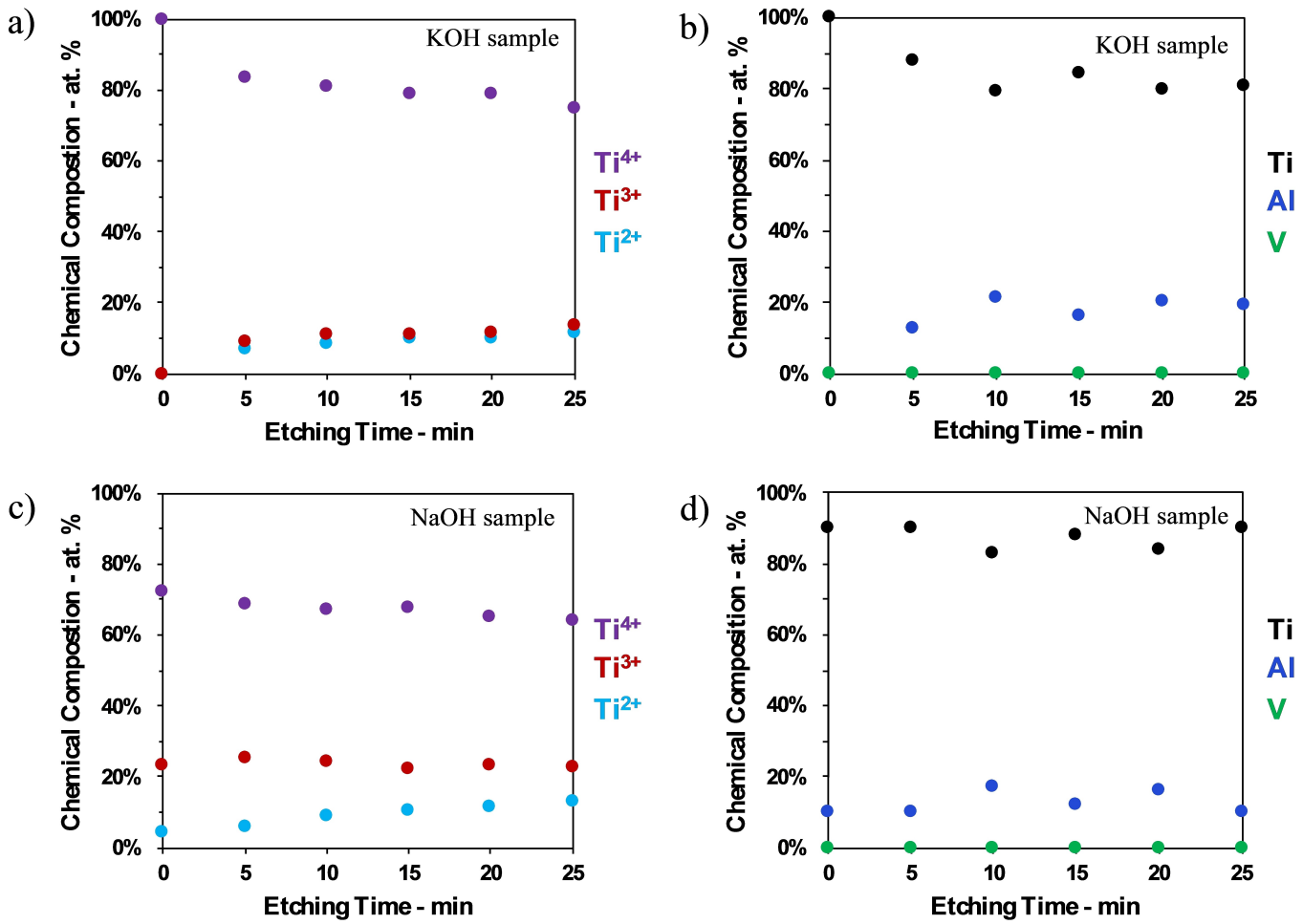


**Figure 9.** a) The Ti species characteristics as a function of the etching time of the KOH sample. b) The atomic concentrations of Ti and Al vary with the etching time while V is still not present after 25 min of etching. c) The Ti species characteristics. d) The atomic concentrations for NaOH.

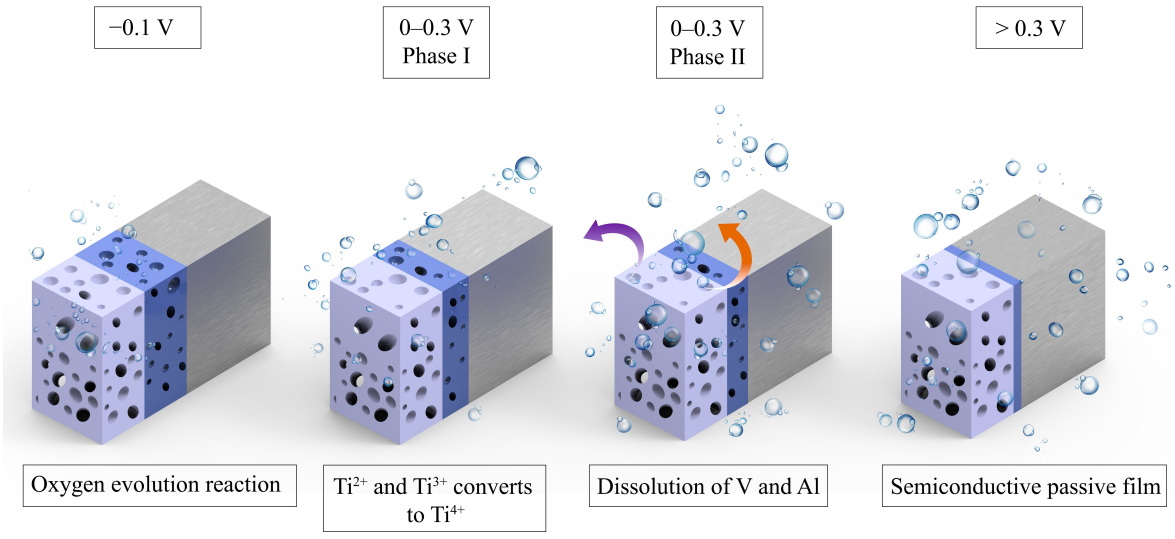


**Figure 10.** The OER mechanism at the AMed Ti-6Al-4V alloy.

film formed on 1 M KOH had a higher ratio of highly charged $Ti^{4+}$ species than the film formed on 1.5 M NaOH (Figures 9a and c). For both samples, the fraction of $Ti^{4+}$ decreased as the sputtering depth increased, while the fraction of $Ti^{2+}$ increased.

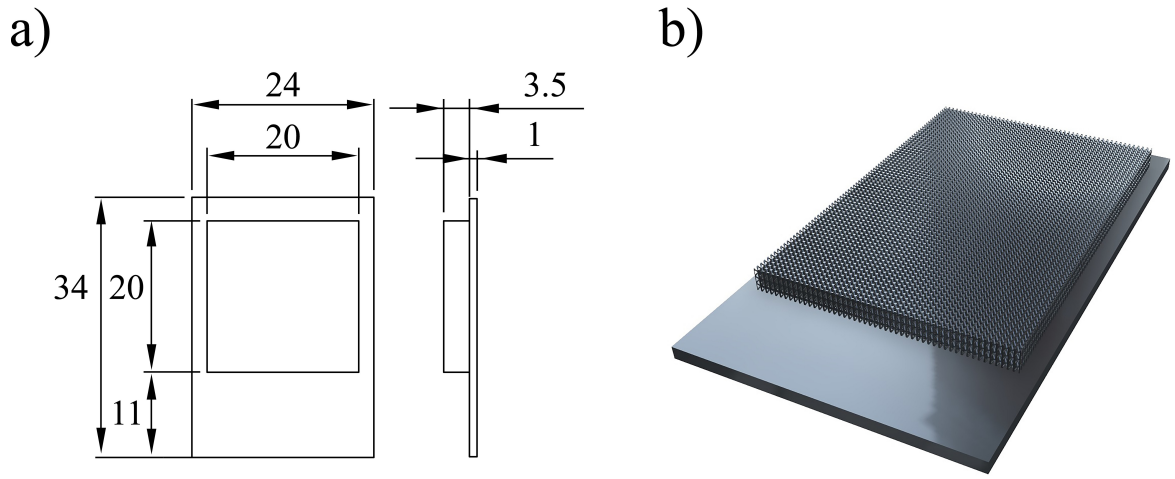


**Figure 11.** A) Dimensions and b) 3D CAD design of the diamond 4 rods Ti-6Al-4V sample.

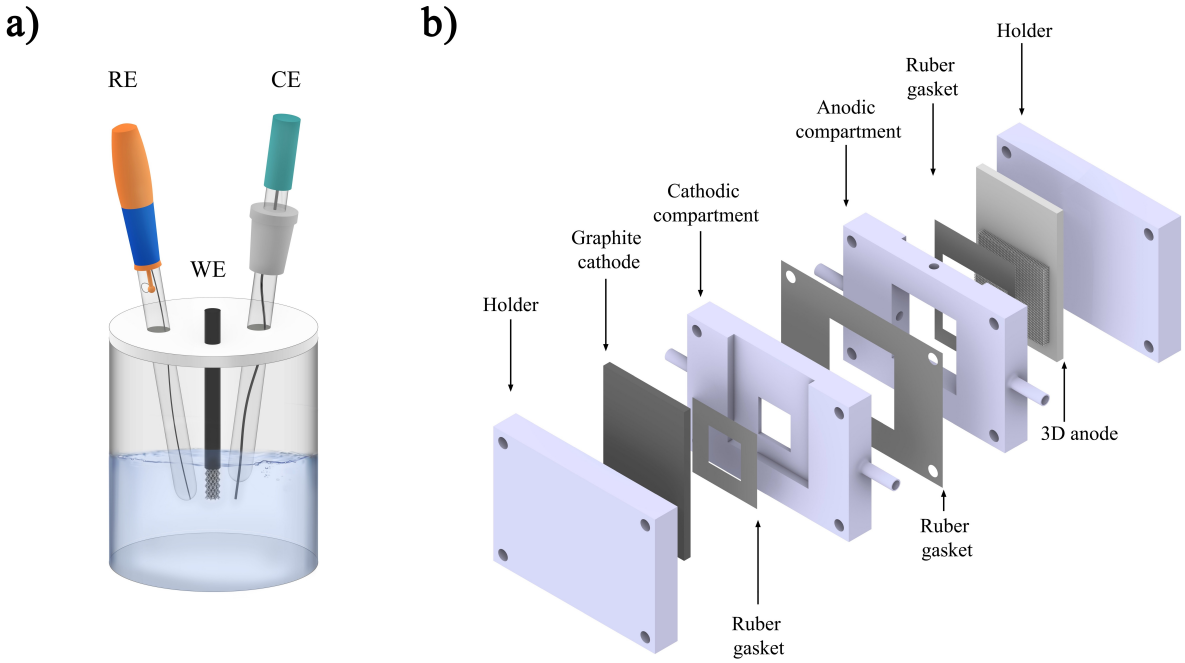


**Figure 12.** Schematics showing a) the static electrochemical condition reactor and b) the advanced flow reactor with dynamic electrochemical conditions.

Depth profiles indicate that the oxide is enriched in aluminum as the surface is etched in both KOH and NaOH samples (Figures 9b and d). Vanadium could not be detected at the sample depths analyzed here. The presence of Al demonstrates that matrix dealloying occurs rapidly for $Al_2O_3$ from the top surface layer of the Ti alloy. This behavior can be attributed to the following plausible reasons: On the one hand, according to the DEIS extracted results (Rct plots), KOH provides higher corrosion–resistance. The porous layer protects the sublayers, which preserve more Al in their structure. As previous studies stated, Al and V could contribute to Ti oxide layers dissolution.[53] Due to the beneficial influence of a mixed passive film composed of Ti, Al, and V oxides on the anodic behavior of the alloy, more straightforward anodic dissolution can be related to better electron transfer through the surface. On the other hand, the out-layer of the KOH sample exhibits a higher corrosion-resistant surface due to the predominant presence of $Ti^{4+}$ ions. Additionally, $Ti^{3+}$, $Ti^{2+}$, and $Al^{3+}$ are unstable ions on the out-layer released from the surface (Figures 9a–c).

Higher $Al^{3+}$ and $Ti^{3+}$ concentrations were identified in the top layer of the sample in 1.5 M NaOH compared to the one in 1 M KOH. Due to the high corrosion kinetics, the presence of Al demonstrates that matrix ion dissolution occurred rapidly for $Al_2O_3$ from the top surface layer in comparison to the one in 1 M KOH. The suppression approach is characterized by aggressive nature of higher alkalinity that enhances the transition of $TiO_2$ to TiO and $Ti_2O_3$. The lower presence of $Ti^{4+}$ might be due to the distortion to $Ti^{3+}$ provided by the high alkalinity. this enhanced local current density by participating in the OER activity of the surface. Therefore, the sample in 1.5 M

NaOH encounters higher corrosion and surface layer dissolution. As a result, the OER probably starts at −0.1 V at the AMed Ti-6Al-4V, and during a transition state range of 0–0.3 V, $Ti^{2+}$ and $Ti^{3+}$ convert to $Ti^{4+}$ at phase I (Figure 10). Then, Phase II may be involved with Al and V dissolutions in the same potential range. Finally, at potentials higher than 0.3 V, a progressive growth of semiconductive passive film occurs.

## Conclusions

A robust and feasible manufacturing method was employed to produce a 3D-microstructured anode. AMed diamond 4 rods scaffold structure of Ti-6Al-4V was proved to be among the most active and feasible noble-metal-free anodes. The present study reveals that the large active surfaces provided by AM diamond 4 rod modify the composition of non-conductive passivation to unstable passivation, possibly providing higher amounts of defects and high wettability. All these effects combined make it ideal for effective charge transfer. Therefore, these uniform 3D-designed structures can improve the catalytic activity of Ti-6Al-4V alloys for OER in advanced flow reactors. The various concentrations of NaOH and KOH solutions were evaluated using different electrochemical approaches. Interestingly, the 4 rod Ti-6Al-4V scaffold structure had 42 times higher electrochemical active surface area than the plate anode. EIS spectra demonstrated that the electrocatalyst kinetics of AMed porous electrodes changed upon electrolyte selection. The alkaline electrolyte caused controllable ion dissolution triggered by a corrosion-controlled medium of Ti-6Al-4V alloys. Based on LSV results, the higher alkalinity generated higher charge transfer up to 911 mA cm$^{-2}$ and 640 mA cm$^{-2}$ for the 1.5 M KOH and 1.5 M NaOH electrolytes, respectively. Charge transfer is eased due to reduced activation energy on the electrode surface, resulting in high anodic dissolution.

In addition, XPS measurements were considered to evaluate the competitive kinetics of Al and V dissolution processes and alloy surface passivation characteristics. The formation of thin barrier-type Ti-, Al-, and V-oxide layers controlled the strong passivating behavior of Ti-6Al-4V alloys. The $S_z$ and $S_a$ parameters indicated the most hydrophilic surface for the 1.5 M NaOH treated sample. The alkaline treatment improved the wettability, smaller bubble formation and faster release from the surface of the studied electrodes. This suggests that anodic reactions on AMed Ti-6Al-4V alloys would be enhanced under these conditions.

As shown in the DEIS exported findings, at 1.5 M NaOH, intensive anodic dissolution, with an increasing number of active sites, promotes charge transfer. However, a 1 M KOH electrolyte showed more corrosion-controlled anodic behavior that reduced charge transfer. In addition, the porous layer covers the sub-layers, thus preserving more Al and possibly V in their structure and extending the lifetime of the electrode. This study demonstrates that AM technology development can be used to design innovative electrodes for significant electrochemical processes. Future work is needed to further address limitations regarding surface deactivation for long-term utilization. In addition, future studies may consider the impact of surface roughness commonly associated with impedance spectroscopy. The interphase and perhaps double layers could have morphological influences, as could impedance spectroscopy.

## Experimental Section

### Material and sample preparation

Ti-6Al-4V fine powders with 63 μm, grade 5 (Sandvik AB) were used to fabricate the anode electrode with Realizer SLM 50 equipment (Realizer GmbH). Potassium hydroxide (ACS reagent, ≥85 %, pellets, Sigma-Aldrich) and 3 N NaOH standard solution were selected as the electrolytes. A Ti-6Al-4V wrought plate, grade 5 (Titanium Joe Inc., Canada) was used for comparing the electrochemical active surface area (ECSA). A diamond 4 rods Ti-6Al-4V electrode with a cylindrical geometry of 0.3117 cm$^2$ and a graphite electrode with 1 cm$^2$ surface area were prepared. In addition, a Ti-6Al-4V plate (cubic rectangular) with 20 mm×20 mm projected area (Figure 11a and b), was used as the primary anode for the flow reactor. The 0.5, 1, and 1.5 M NaOH and KOH electrolytes were considered for electrochemical measurements at room temperature.

### Electrochemical measurements

The electrochemical measurements were done using an Autolab PGSTAT 302N potentiostat (Metrohm). Ti-6Al-4V specimens were ultrasonically cleaned. The Ag/AgCl electrode (SENTEK R1/AG/4MM, and eDAQ ET073, 2 mm diameter) was used as the reference electrode and a Pt wire electrode (Metrohm, Ref [6].0301.100) as the counter electrode in both static and dynamic conditions.

Cyclic voltammetry of samples was acquired in 0.5 M NaOH in non-faradic regions of samples. Capacitance measurements were used to estimate the ECSA of the wrought plate and AMed 4 rods electrodes. Different cyclic voltammetry (CV) scan rates were measured in the non-faradic region to evaluate the ECSA. The linear fitted slope of the anodic ($j_a$) and cathodic current densities differences ($\Delta j = (j_a - j_c)$) were determined at a certain potential range versus scan rates equals the double-layer capacitance ($C_{dl}$), which is proportional to the effective electrode surface area. $C_{dl}$ was calculated by plotting the difference in cathodic and anodic charging currents in a non-Faradaic region of the potential window against 5 to 100 mV s$^{-1}$ rates. Furthermore, the $C_{dl}$ plotted curves demonstrated the double layer capacitance difference between the scaffold geometry and the plate. It is possible to compare the comparative surface areas of electrodes with varied geometries using the slopes of these fitting lines. This is mainly when these electrodes are manufactured from the same material.

Tafel tests were carried out at a 0.5 mV/s scan rate from −250 mV to 250 mV versus open circuit potential ($V_{OCP}$). Further, linear sweep voltammetry (LSV) was acquired at 2 mV/s. Before the potentiodynamic polarization measurements, the samples were pretreated with a standard oxide removal procedure for Ti-6Al-4V.[40] The first step was degreasing in 1 M NaOH solution for 1 min, followed by acid dipping in HCl 50 % by volume for 15 min. The surface was then activated by a mixture of acids ($HNO_3$ 30 % by volume and HF 50 % v/v) for 1 min. The fourth step inhibited oxide layer formation by immersion in HF 12.5 % v/v plus $CH_3COOH$ for 15 minutes. All the steps followed by rinsing with deionized water. Moreover, the samples were immersed in the targeted alkaline electrolyte (NaOH and/or KOH) for one hour to stabilize.

Electrochemical impedance spectroscopy (EIS) is an effective analysis technique since it removes interference from diffusion effects.[41] In order to obtain more stable trends, samples were kept in targeted NaOH and KOH solutions for 24 hours prior to EIS and DEIS measurements. The frequency range was 10 Hz–100 kHz, and the excitation signal amplitude was 10 mV. The plots were then assessed by Tafel fitting. To analyze the data from the EIS and DEIS, Zview® software was used. After evaluating the static electrochemical conditions with a non-flow reactor (Figure 12a), the advanced flow reactor was used to evaluate the effects of alkaline flow on the anodic behavior of the electrode. The advanced flow reactor provides dynamic electrochemical conditions and was operated with a flow rate of 40 mL $min^{-1}$ for 4 hours with an applied current density of 180 mA $cm^{-2}$ (Figure 12b).

### Surface and structure Characterizations

3D-designed electrodes with a projected surface area of 4 $cm^2$ were utilized for surface analysis. The surface morphology and roughness were studied using a 3D laser scanning microscope (Keyence VR-3200; KEYENCE, Osaka, Japan), with a measuring resolution of 0.5 μm on the Z-axis.[41] Imaging of the structural 3D-printed design of the Ti-6Al-4V sample was obtained by SEM (Hitachi SU 3500, Japan). XPS analysis was carried out with a PHI 5000 VersaProbe III spectrometer equipped with a monochromatic AlKα source. Narrow scan measurements were acquired with dual charge compensation and aligned with the adventitious carbon peak (C1s) at 284.8 eV before analysis. Etching of the surface was carried out with a 1 kV beam energy, 3 mm×3 mm raster size and an etch rate of 10.5 Å/min with reference to $Ta_2O_5$.

## Acknowledgements

The authors acknowledge the Academy of Finland ReGold-AM project (Grant No. 325002), Emil Aaltonen, K.H. Renlund foundation, and Walterahlström Foundation for the financial support of this project. The authors gratefully acknowledge Dr. Marina Aghayan and Dr. Ali Saffar Shamshirgar from Fact-Industries Inc. for the helpful advice and Additive Manufacturing of the electrodes.

## Conflict of Interests

The authors declare no conflict of interest.

## Data Availability Statement

The data that support the findings of this study are available from the corresponding author upon reasonable request.

**Keywords:** alkaline electrolysis · anodic behavior · dynamic impedance spectroscopy · 3D printing · Ti-6Al-4V

[1] I. Korolev, P. Altınkaya, P. Halli, P. M. Hannula, K. Yliniemi, M. Lundström, *J. Cleaner Prod.* **2018**, *186*, 840–850.
[2] M. Laatikainen, I. Makarova, T. Sainio, E. Repo, *Sep. Purif. Technol.* **2022**, *278*, 119571.
[3] I. Korolev, P. Altinkaya, M. Haapalainen, E. Kolehmainen, K. Yliniemi, M. Lundström, *Chem. Eng. J.* **2022**, *429*, 1–11.
[4] H. Zhang, Y. Luo, P. K. Chu, Q. Liu, X. Liu, S. Zhang, J. Luo, X. Wang, G. Hu, *J. Alloys Compd.* **2022**, *922*, 166113.
[5] J. Liu, S. Duan, H. Shi, T. Wang, X. Yang, Y. Huang, G. Wu, Q. Li, *Angew. Chem.* **2022**, *134*, e202210753.
[6] S. C. Perry, C. Ponce de León, F. C. Walsh, *J. Electrochem. Soc.* **2020**, *167*, 155525.
[7] Y. Wen, T. Zhang, J. Wang, Z. Pan, T. Wang, H. Yamashita, X. Qian, Y. Zhao, *Angew. Chem.* **2022**, *134*, e202205972.
[8] K. Amini, A. Sadeghi, M. Pritzker, J. Gostick, *J. Porous Electrodes in Redox Flow Batteries* **2022**, 466–479.
[9] S. L. Sing, S. Huang, G. D. Goh, G. L. Goh, C. F. Tey, J. H. K. Tan, W. Y. Yeong, *Prog. Mater. Sci.* **2021**, *119*, 100795.
[10] P. Nyamekye, P. Nieminen, M. R. Bilesan, E. Repo, H. Piili, A. Salminen, *Appl. Mater. Today* **2021**, *23*, 101040.
[11] S. Chang, X. Huang, C. Y. Aaron Ong, L. Zhao, L. Li, X. Wang, J. Ding, *J. Mater. Chem. A* **2019**, *7*, 18338–18347.
[12] J. Li, X. Lin, M. Zheng, J. Wang, P. Guo, T. Qin, M. Zhu, W. Huang, H. Yang, *Electrochim. Acta* **2018**, *283*, 1482–1489.
[13] N. Dai, L. C. Zhang, J. Zhang, X. Zhang, Q. Ni, Y. Chen, M. Wu, C. Yang, *Corros. Sci.* **2016**, *111*, 703–710.
[14] G. A. Longhitano, M. A. Arenas, A. Conde, M. A. Larosa, A. L. Jardini, C. A. de C. Zavaglia, J. J. Damborenea, *J. Alloys Compd.* **2018**, *765*, 961–968.
[15] A. Sharma, M. C. Oh, J. T. Kim, A. K. Srivastava, B. Ahn, *J. Alloys Compd.* **2020**, *830*, 154620.
[16] M. Kahvazi, M. Yeganeh, M. Tavakoli, **2022**, *31*.
[17] Z. Yu, Z. Chen, D. Qu, S. Qu, H. Wang, F. Zhao, C. Zhang, A. Feng, D. Chen, *Materials* **2022**, *15*, 4473.
[18] S. Liu, Y. C. Shin, *Mater. Des.* **2019**, *164*, 107552.
[19] Y. Xu, S. Wu, P. Wan, J. Sun, Z. D. Hood, *RSC Adv.* **2017**, *7*, 32461–32467.
[20] C. Kim, M. R. Kendall, M. A. Miller, C. L. Long, P. R. Larson, M. B. Humphrey, A. S. Madden, A. C. Tas, *Mater. Sci. Eng. C* **2013**, *33*, 327–339.
[21] Q. Wang, Y. Cheng, H. B. Tao, Y. Liu, X. Ma, D. S. Li, H. B. Yang, B. Liu, *Angew. Chem. Int. Ed.* **2023**, *135*, e202216645.
[22] D. Zhang, J. Yang, P. Gan, W. Zhang, in (Eds.: L. Guo, C. Verma, D. B. T.-E.-F. C. I. Zhang), Elsevier, **2022**, pp. 55–70.
[23] H. KAMINAKA, Nippon Steel Sumitomo Met. Tech. Rep. **2014**, 104.
[24] M. G. Fontana, *Ind. Eng. Chem.* **1947**, *39*, 91A-92A.
[25] N. Zaveri, G. D. McEwen, R. Karpagavalli, A. Zhou, *J. Nanopart. Res.* **2010**, *12*, 1609–1623.
[26] W. Q. Yu, J. Qiu, L. Xu, F. Q. Zhang, *Biomed. Mater.* **2009**, *4*.
[27] Y. Okazaki, S. Rao, Y. Ito, T. Tateishi, *Biomaterials* **1998**, *19*, 1197–1215.
[28] N. L. Hernández de Gatica, G. L. Jones, J. A. Gardella, *Appl. Surf. Sci.* **1993**, *68*, 107–121.
[29] M. T. Pham, I. Zyganow, W. Matz, H. Reuther, S. Oswald, E. Richter, E. Wieser, *Thin Solid Films* **1997**, *310*, 251–259.
[30] N. Ibriş, J. C. Mirza Rosca, *J. Electroanal. Chem.* **2002**, *526*, 53–62.
[31] C. Science, G. Britain, M. Science, N. Ng, **1988**, *28*, 43–56.
[32] J. Yahalom, J. Zahavi, *Electrochim. Acta* **1971**, *16*, 603–607.
[33] J. F. Vanhumbeeck, L. Ryelandt, J. Proost, *Electrochim. Acta* **2009**, *54*, 3330–3338.
[34] T. Shibata, Y. C. Zhu, *Corros. Sci.* **1995**, *37*, 133–144.
[35] J.-H. Xing, Z.-B. Xia, J.-F. Hu, Y.-H. Zhang, L. Zhong, *J. Electrochem. Soc.* **2013**, *160*, C239–C246.
[36] A. Ishihara, C. Wu, T. Nagai, K. Ohara, K. Nakada, K. Matsuzawa, T. Napporn, M. Arao, Y. Kuroda, S. Tominaka, S. Mitsushima, H. Imai, K. ichiro Ota, *Electrochim. Acta* **2018**, *283*, 1779–1788.
[37] Y. Xiao, N. Dai, Y. Chen, J. Zhang, S. W. Choi, *Mater. Res. Express* **2019**, *6*, 126521.
[38] L. O. Berbel, E. D. P. Banczek, I. K. Karoussis, G. A. Kotsakis, I. Costa, *PLoS One* **2019**, *14*, 1–17.
[39] M. Diffuser, S. Nur, A. Shafie, W. Y. Shen, J. J. Jaymon, N. Abdul, H. Nordin, M. Hafiz, D. Othman, J. Jaafar, A. F. Ismail, **2022**, 1–13.
[40] S. T. Bill F. Rothschild, Method for Plating on Titanium. **1990**, No. 4,938,850.
[41] M. A. Goulet, M. Skyllas-Kazacos, E. Kjeang, *Carbon* **2016**, *101*, 390–398.
[42] Y. Zhang, J. Li, H. Xu, L. Feng, T. Zhang, *J. Alloys Compd.* **2020**, *849*, 156622.
[43] M. Fazel, H. R. Salimijazi, M. A. Golozar, M. R. Garsivaz Jazi, *Appl. Surf. Sci.* **2015**, *324*, 751–756.
[44] N. Zakerin, K. Morshed-Behbahani, *J. Mol. Liq.* **2021**, *333*, 115947.
[45] M. Aziz-Kerrzo, K. G. Conroy, A. M. Fenelon, S. T. Farrell, C. B. Breslin, *Biomaterials* **2001**, *22*, 1531–1539.

[46] W. A. Badawy, A. M. Fathi, R. M. El-Sherief, S. A. Fadl-Allah, *J. Alloys Compd.* **2009**, *475*, 911–916.
[47] S. Tamilselvi, V. Raman, N. Rajendran, *Corros. Eng. Sci. Technol.* **2011**, *46*, 585–591.
[48] F. E. T. Heakal, O. S. Shehata, *Prot. Met.* **2020**, *56*, 333–342.
[49] Y. Bai, X. Gai, S. Li, L. C. Zhang, Y. Liu, Y. Hao, X. Zhang, R. Yang, Y. Gao, *Corros. Sci.* **2017**, *123*, 289–296.
[50] V. A. Alves, R. Q. Reis, I. C. B. Santos, D. G. Souza, T. de, M. A. Pereira-da-Silva, A. Rossi, L. A. da Silva, *Corros. Sci.* **2009**, *51*, 2473–2482.
[51] Y. Cai, W. Chang, X. Luo, A. M. L. Sousa, K. H. A. Lau, Y. Qin, *Precis. Eng.* **2018**, *52*, 266–275.
[52] T. Shibata, Y. C. Zhu, *Corros. Sci.* **1995**, *37*, 253–270.
[53] H. Krawiec, V. Vignal, J. Loch, P. Erazmus-Vignal, *Corros. Sci.* **2015**, *96*, 160–170.

Manuscript received: July 10, 2023
Revised manuscript received: August 31, 2023
Version of record online: ■■, ■■

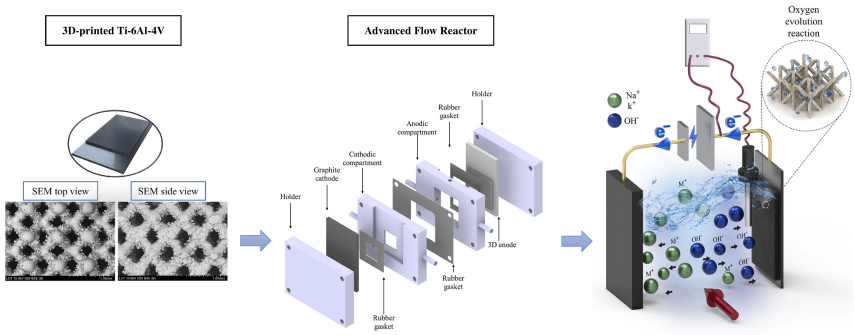


*M. Reza Bilesan*, M. Yazdani, Asst. Prof. M. Luneau, Dr. G. Montserrat-Sisó, Assoc. Prof. B. Wickman, Prof. E. Repo*

1 – 15

## Electrochemical Approach for Advanced Flow Reactors via Additive Manufacturing of High Surface Area Ti-6Al-4V Anode

**Noble-free 3D anode**: 3D-printed Ti-6Al-4V electrode was evaluated for its anodic behavior in alkaline solutions with a novel electrochemical approach. According to the ECSA results from voltammetry, 3D Ti-6Al-4V provides 42 times more active surface area than flat plate anodes. It enables effective charge transfer of 911 mA cm$^{-2}$ from almost non-conductive anodic behavior of a plate structure.